Investigation of Sulfated Iron-Based Catalysts with Different Sulfate Position for Selective Catalytic Reduction of NO$_x$ with NH$_3$

Baiyu Fan [1], Ziyin Zhang [2], Caixia Liu [1,*] and Qingling Liu [1]

[1] School of Environmental Science and Engineering, Tianjin University, Tianjin 300072, China; fanbaiyu@tju.edu.cn (B.F.); liuql@tju.edu.cn (Q.L.)

[2] Langfang City Beichen Entrepreneurship Resin Materials Incorporated Company, Langfang 065000, China; laowuzhangziyin@163.com

* Correspondence: liucx@tju.edu.cn; Tel.: +86-13426103078

Abstract: The Fe/(SZr) and S(Fe/Zr) sulfated iron-based catalysts, prepared by impregnation methods through changing the loading order of Fe$_2$O$_3$ and SO$_4{}^{2-}$ on ZrO$_2$, were investigated on selective catalytic reduction (SCR) of NO$_x$ by ammonia. It was studied that the existent forms of Fe$_2$O$_3$ and SO$_4{}^{2-}$ on the surface of catalysts were affected by the loading order. The Fe/(SZr) catalyst surface had isolated Fe$_2$O$_3$ and SO$_4{}^{2-}$ species and followed both the L-H mechanism and the E-R mechanism, whereas the S(Fe/Zr) catalyst contained SO$_4{}^{2-}$ specie and sulfate only and mainly followed the E-R pathway. These factors affected the redox ability and NH$_3$ adsorption, which might be key to the SCR reaction.

Keywords: iron-based catalysts; sulfated; selective catalytic reduction; NO$_x$ abatement

1. Introduction

Nitrogen oxides usually come from stationary sources, such as coal-fired power plants, industrial boilers, and mobile sources, like diesel engines and marine engines. They have caused lots of harmful problems to the ecosystem health. For example, the acid rain would dissolve toxic metals into the water, resulting in reducing species. The photochemical smog could harm plants and reduce atmospheric visibility. Besides, nitrogen oxides made people face existential threats. The resulting photochemical fumes could irritate the eyes, invade the lungs, and even cause death. Therefore, it is important to remove nitrogen oxides. Currently, selective catalytic reduction of NO$_x$ by ammonia (NH$_3$-SCR) is an efficient technology to abate NO$_x$ in the flue gas from stationary sources [1]. The core of this method is catalysts. Typically, the V$_2$O$_5$-WO$_3$/TiO$_2$ is the most commonly used catalysts [2]. However, there are still some shortcomings of vanadium-based catalysts that need to be addressed, including the narrow temperature window, the low N$_2$ selectivity at high temperatures, losing SCR activity by SO$_2$ poisoned, and the secondary pollution to the environment. Due to these disadvantages, the development of other metals for vanadium and the modification of the support have been investigated over the past several decades. Iron-based catalysts have received considerable attention for its well NH$_3$-SCR activity and N$_2$ selectivity, such as α-Fe$_2$O$_3$ [3], γ-Fe$_2$O$_3$ [3], MgFe$_2$O$_4$ [4], Fe$_2$O$_3$/SiO$_2$ [5], Fe$_2$O$_3$/TiO$_2$ [6], Fe$_2$O$_3$/TiO$_2$-pillared clays [1], Fe-ZSM5 [7], and Fe-MOR [8]. Besides iron-based catalysts, other sulfated catalysts were reported to be active for SCR reaction. Grange et al. [9,10] reported that V$_2$O$_5$-WO$_3$ catalyst supported on TiO$_2$-SO$_4{}^{2-}$ extended high activity up to 450 °C, and for sulfate, increased the acid sites and improved the interaction between V$_2$O$_5$ and WO$_3$. Ke et al. [11] reported that cobalt sulfate exhibited high NO$_x$ conversion and well resistance to H$_2$O and SO$_2$ poisoning, because the existence of sulfate reduced the number of bulk Co$_3$O$_4$ and cooperated with cobalt oxides to improve

the activity of SCR reaction. Gu et al. [12] reported that sulfated CeO_2 possessed high NO_x conversion and N_2 selectivity in the temperature range of 200–570 °C, and suggested that sulfate enhanced the active oxygen species and NH_3 adsorption on surface, which were responsible for the higher reactivity of sulfated CeO_2.

The iron-based oxide and sulfate catalysts for SCR of NO_x by NH_3 have been investigated in recent years. However, few studies have been performed on the preparation process about sulfating. In this study, a series of sulfated iron-based catalysts were prepared through different sulfate-loaded order and characterized by XRD, BET, XPS, Raman, and NH_3-TPD. The high activities of sulfated iron-base catalysts were also explained on the basis of the characterization results.

2. Results

2.1. SCR Catalytic Activity and Influence of SO_2

The activity curves of the sulfated iron-based catalysts are shown in Figure 1a. The Fe/Zr catalyst exhibited the lowest activity in the temperature range of 150–500 °C, and its NO_x conversion reached the highest 46.6% at 350 °C and the NO_x conversion decreased sharply to negative value in the temperature range of 400–500 °C, which was attributed to the NH_3 oxidation to NO_x at the high temperature. Notably, the activities of sulfated iron-based catalysts improved remarkably in the temperature range of 250–500 °C compared with Fe/Zr catalyst. The NO_x conversion of Fe/(SZr) catalyst reached above 90% in 300–450 °C, amazingly, the NO_x conversions increased to 98%, but which decreased to 50% at 500 °C. The temperature window of NO_x conversion of Fe/(SZr) catalysts became narrow and moved to high temperature. The NO_x conversion of Fe/(SZr) catalyst was reached 90% at 400–450 °C. The SCR reaction of the catalysts mainly follows the Eley−Rideal (E-R) mechanism and/or Langmuir–Hinshelwood mechanism (L-H) [13,14]. It is the critical reaction step to adsorb NH_3 to form activated ammonia species on the catalyst and then react with NO or adsorbed oxynitride species to generate N_2 and H_2O. Therefore, the acidic sites are key for the SCR reaction. The sulfated iron-based catalysts were prepared by adding SO_4^{2-}, which could remarkably increase the acidic sites. Therefore, the activity improves obviously with the sulfated iron-based catalyst.

The N_2 selectivity is one of the important indicators for the activities of NO_x selective catalytic reduction by NH_3. The N_2 selectivity of Fe/Zr, Fe/(SZr), and S(Fe/Zr) is showed in Figure 1b. S(Fe/Zr) showed excellent N_2 selectivity in 150–500 °C. The N_2 selectivity of Fe/Zr catalyst decreased from 250 °C, and the N_2 selectivity of Fe/Zr catalyst dropped greatly at 500 °C to 88%. The slight decrease in N_2 selectivity in the high temperature range might be due to the higher ability of oxidization of NH_3 to NO [15], which resulted in less production of N_2. Besides, according to He et al. [16], the intermediate specie -HNO would combine with -NH to produce N_2O after the oxidization of NH_3, which led to less N_2 selectivity.

As shown in Figure 1c, this work investigated the effect of SO_2 on the activity of Fe/(SZr) and S(Fe/Zr) catalysts. In the figure, the activity of the S(Fe/Zr) catalyst remained stable for 840 min in the presence of SO_2, but the NO_x conversion rate was relatively low. For the Fe/(SZr) catalyst, the de-NO_x reactivity slightly decreased and the NO_x conversion rate kept stable between 770 and 840 min when there was SO_2. This demonstrated that the Fe/(SZr) catalyst had superior SO_2 tolerance and exhibited higher activity. Typically, it was recognized that the Langmuir–Hinshelwood (L-H) mechanism or/and Eley–Rideal (E-R) mechanism were followed by catalysts during the reaction [17]. Meanwhile, it could be assumed that there was competitive adsorption between SO_2 and NO, in which SO_2 was easier to adsorb than the other. Therefore, the Langmuir–Hinshelwood (L-H) mechanism was suppressed, but the Eley–Rideal (E-R) mechanism still existed on the Fe/(SZr) catalyst. It was the reason that Fe/(SZr) had stronger SO_2 resistance. These would be analyzed in more detail in Discussion section.
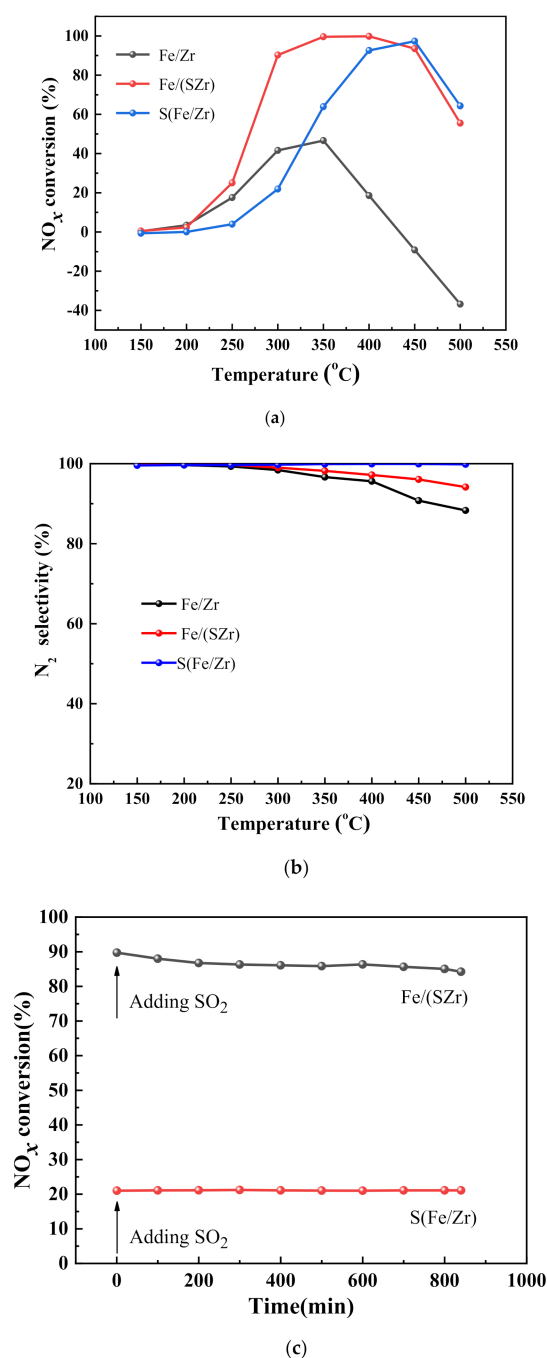
(a)

(b)

(c)

Figure 1. (**a**)NH$_3$–selective catalytic reduction (SCR) activity, (**b**) N$_2$ selectivity, and (**c**) influence of SO$_2$ on NO$_x$ conversion of Fe/Zr, Fe/(SZr), and S(Fe/Zr) for the NO$_x$ reduction with NH$_3$.

2.2. XRD

XRD patterns of the ZrO$_2$, α-Fe$_2$O$_3$, Fe/Zr, Fe/(SZr), and S(Fe/Zr) catalysts are shown in the Figure 2. Both the ZrO$_2$ and α-Fe$_2$O$_3$ showed obvious characteristic peaks. However, the patterns of Fe/Zr, Fe/(SZr), and S(Fe/Zr) exhibited only one phase, which corresponded to the cubic crystal structure of ZrO$_2$. In other words, the X-ray diffraction peaks of α-Fe$_2$O$_3$ or Fe$_2$(SO$_4$)$_3$ did not appear in the patterns, which demonstrated that Fe$_2$O$_3$ and SO$_4^{2-}$ dispersed well on the surface of ZrO$_2$. According to references [15,18], the shape of peaks would be changed or new peak would appear if Fe$_2$O$_3$ or/and SO$_4^{2-}$ entered into the crystal ZrO$_2$. These proved that the sulfating process did not affect the crystal form of Fe/Zr, Fe/(SZr), and S(Fe/Zr) catalysts. In fact, the change of crystal structure

and high dispersion had significant influences on the catalytic performance [15], which might affect the existent forms of active species and pathways followed on catalysts.
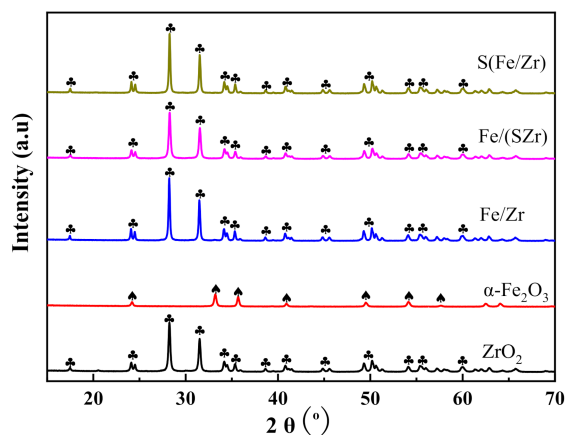

Figure 2. XRD patterns of different iron-based catalysts.

2.3. BET and ICP

It is well known that the surface area is crucial to catalytic activity because large surface area could facilitate to well dispersion. However, the surface areas of sulfated iron-based catalysts were so low (Table 1) that the distinction among them could be neglected. Meanwhile, integra mass concentrations of Fe, S, and Zr measured by the ICP equipment are also summarized in Table 1. The integra mass concentrations of Fe, S, and Zr were close to their calculated values.

Table 1. Brunauer-Emmett-Teller (BET) surface area and integral mass concentration of various catalysts by Inductive Coupled Plasma (ICP) results.

Sample	Integral Mass Concentration (wt.%)			Surface Area(m^2/g)
	Fe	S	Zr	
Fe/(SZr)	2.0	1.4	64.5	1.1
S (Fe/Zr)	2.1	1.3	63.4	1.2

2.4. Raman

To investigate the species on the surface of sulfated iron-based catalysts, the Raman spectra were collected at room temperature. Figure 3 showed the Raman spectra of different sulfated iron-based catalysts and pure Fe_2O_3. The Fe/(SZr), S(Fe/Zr), and ZrO_2 catalysts all showed similar peak shapes, but the strength was different in the wavenumber range of 0–650 cm^{-1}, which meant that the sulfate and Fe_2O_3 species on catalyst surfaces did not have effects on ZrO_2. Besides, several bands in the range of 800–1500 cm^{-1} were detected, in which the peak centered at 1278 cm^{-1} on Fe/(SZr) was assigned the fingerprint peak of Fe_2O_3 [19]. There was no characteristic peak in the range of 800–1500 cm^{-1} on ZrO_2. Only one peak appeared at 992 cm^{-1} on the surface of S(Fe/Zr) catalyst, which was assigned to the S=O bands of isolated sulfate. For Fe/(SZr) catalyst, three peaks located at 992, 1082, and 1278 cm^{-1} could be detected, respectively. Among them, the band at 1082 cm^{-1} was induced by the S=O bond of the polynuclear sulfate type [10]. These demonstrated that species such as Fe_2O_3, isolated SO_4^{2-}, and sulfate existed on Fe/(SZr) catalyst. In short, it could be concluded that the S(Fe/Zr) catalyst surface had isolated SO_4^{2-} and sulfate because of the different sulfation preparation processes, which led to different species on the surface of catalysts. These affected the mechanisms followed by catalysts.
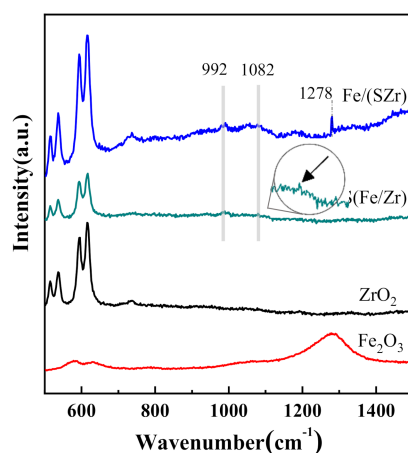
Figure 3. Raman patterns of different iron-based catalysts.

2.5. XPS

X-ray photoelectron spectroscopy (XPS) was used to characterize chemical states and surface atomic concentrations of Fe, O, S, and Zr elements on Fe/(SZr) and S(Fe/Zr) catalysts. Peaks were fitted by Gaussian–Lorentz curves [20]. These results are shown in Figure 4. Meanwhile, the surface atomic concentrations of Fe, S, and Zr are summarized in Table 2.
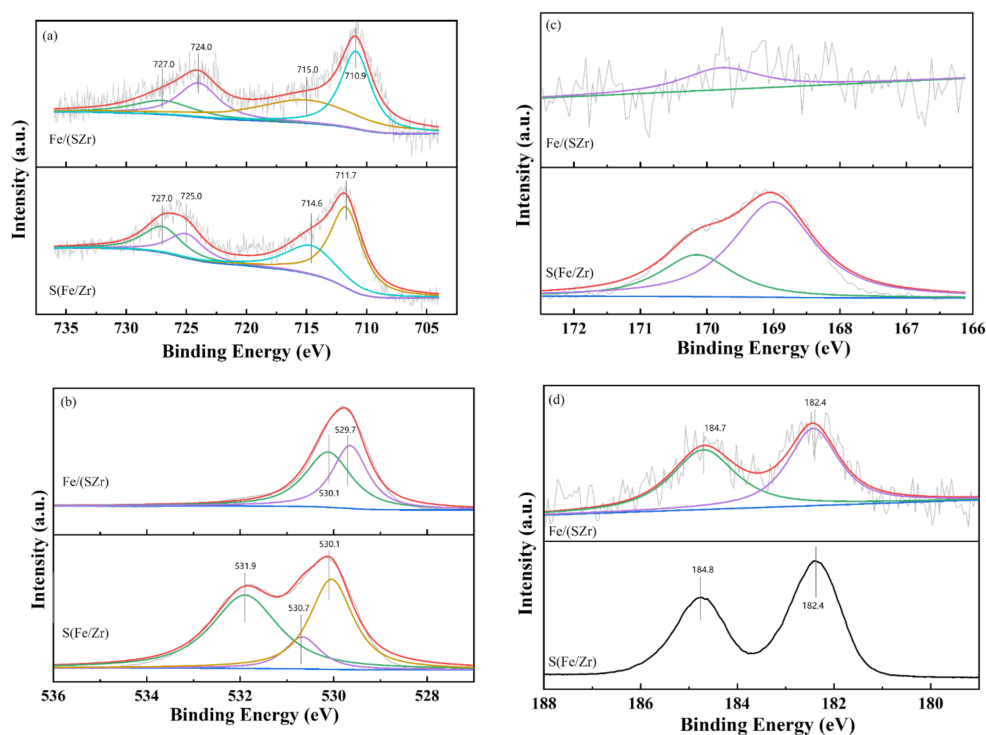

Figure 4. XPS results of (**a**) Fe 2p, (**b**) O 1s, (**c**) S 2p, and (**d**) Zr 3d in Fe/(SZr) and S (Fe/Zr) catalysts.

Table 2. Surface atomic concentration of various catalysts by XPS results.

Sample	Surface Atomic Concentration (%)			
	Fe	O	S	Zr
Fe/(SZr)	1.7	77.1	0.3	0.3
S(Fe/Zr)	3.2	60.9	4.8	15.9

The curves of Fe2p are displayed in the Figure 4a. The peak located at 727.0 eV was corresponded to the Fe2p$_{1/2}$ of Fe^{3+}, and peaks referred to the Fe2p$_{3/2}$ of Fe^{3+} were at the banding energy of 710.9 and 711.7 eV. Besides, the banding energy at 724.0 and 725.0 eV were corresponded to the Fe2p$_{1/2}$ of Fe^{2+}. According to the previous studies [18], the peaks at 715.0 and 714.6 eV were identified as the fingerprint peak influenced by SO$_4^{2-}$. The ratio of Fe^{3+}/(Fe^{2+} + Fe^{3+}) on Fe/(SZr) was 69.6%, which was larger than that of S(Fe/Zr) (58.1%). It was known that the catalyst surface containing more Fe^{3+} species would exhibit better performances during the redox reaction because the transformation between Fe^{2+} and Fe^{3+} could irritate the redox circle, which agreed with the results of SCR catalytic activity. Besides, these results also indicated that the main specie on the surface of Fe/(SZr) was Fe$_2$O$_3$, corresponding to the Raman results.

Additionally, Figure 4b showed the XPS results of O 1s. The profiles of O 1s exhibited large differences between Fe/(SZr) and S(Fe/Zr) catalysts. For the Fe/(SZr) catalyst, the two peaks appeared at 530.1 and 529.7 eV. The banding energy at 530.1 eV was attributed to the surface-chemisorbed labile oxygen (denoted as O_α), and the 529.7 eV peak was corresponded to the lattice oxygen (denoted as O_β) [21]. However, three peaks located at 531.9, 530.7, and 530.1 eV could be observed on the S(Fe/Zr) catalyst, which demonstrated that there were three forms of oxygen on this catalyst. In addition to the surface-chemisorbed oxygen and the lattice oxygen, the O$_2^{2-}$ contained in the SO$_4^{2-}$ species led to the appearance of the peak located at 531.9 eV, which was in accordance with our previous research [2]. Typically, the surface-chemisorbed labile oxygen played important roles in the SCR reaction. More the content of O_α, the higher catalytic activity of catalysts because the surface oxygen (Oα) could promote the activation of NH$_2^-$ formed by NH$_3$ due to the more efficient mobility of electrons than lattice oxygen [21]. Therefore, the Fe/(SZr) catalyst had superior redox activity. For Fe/(SZr) catalyst, the content of O_α/(O_α + O_β) was 53.5%, which was higher than that of S(Fe/Zr) (22.7%). This meant that Fe/(SZr) had better redox ability in the SCR reaction, which was in accordance with the results of SCR catalytic activity and H$_2$–TPR.

The XPS results of S 2p are shown in Figure 4c. For Fe/(SZr), the peak representing S was unconspicuous. However, two obvious peaks could be detected on S(Fe/Zr) catalyst. The banding energy at 170.1 and 169.0 eV was referred to the S^{6+} in SO$_4^{2-}$ [22]. These results manifested that the main species on the surface of Fe/(SZr) was Fe$_2$O$_3$. Although the isolated SO$_4^{2-}$ species existed on the Fe/(SZr) catalyst, the surface atomic concentration was extremely low (only 0.3%) (Table 1). It was because XPS detected the surface atomic concentration and only a small amount of SO$_4^{2-}$ existed on the surface, although SO$_4^{2-}$ was the main species on the surface of S(Fe/Zr). These results corresponded with the O 1s results.

The XPS spectra of Zr 3d are presented in Figure 4d. Each catalyst was fitted with two characteristic peaks. For the Fe/(SZr) catalyst, the banding energy located at 184.8 eV was corresponded with the Zr 3d$_{3/2}$. Another peak at 182.4 eV was referred to the Zr^{4+} species. The positions of peaks were similar, which certified that the existence of Zr species was stable and not affected by the sulfating process.

The ICP results demonstrated that the integral mass concentrations of Fe, S, and Zr were all extremely similar for sulfated iron-based catalysts. Combined with the XPS results of concentrations of virous elements, it could be concluded that the preparation method of Fe/(SZr) and S(Fe/Zr) merely affected the surface atomic concentrations, rather than the integral atomic concentrations.

2.6. H$_2$–TPR

H$_2$–TPR technique was used to investigate the interaction between Fe$_2$O$_3$ and SO$_4^{2-}$. The H$_2$–TPR curves of all the catalysts are shown in Figure 5. The profile of Fe/Zr showed three peaks centered at 329, 417, and 540 °C. The peaks at 329 and 522 °C could be attributed to the reduction of the surface Fe$_2$O$_3$ (Fe$_2$O$_3$–Fe$_3$O$_4$–Fe) [23], and another peak at 417 °C could be assigned to the peak produced by the machine. However, for the other three catalysts, the intensity of this peak was too slight too be observed. The pattern of SZr showed only one peak centered at 585 °C, which corresponded to the reduction of SO$_4^{2-}$ [24]. The H$_2$–TPR curves of Fe/(SZr) and S(Fe/Zr) showed only one peak,

which centered at 403 and 486 °C, respectively. Their reduction peak temperature (T_{red}) were all higher than that of Fe/Zr catalyst and lower than that of SZr catalyst, which were referred to the overlapping of the stepwise reduction peaks of Fe_2O_3 and SO_4^{2-}. According to reference [25], lower the T_{red} is, the stronger is the redox ability of the catalyst. Among Fe/(SZr) and S(Fe/Zr) catalysts, the redox abilities were as following: Fe/(SZr) > S(Fe/Zr). By combining the Raman results, it was concluded that the surface species were different because of the different sulfated order. In other words, the existent forms of Fe_2O_3 and SO_4^{2-} on the surface of ZrO_2 resulted in the different interaction of Fe_2O_3 and SO_4^{2-}, which impacted the redox ability.
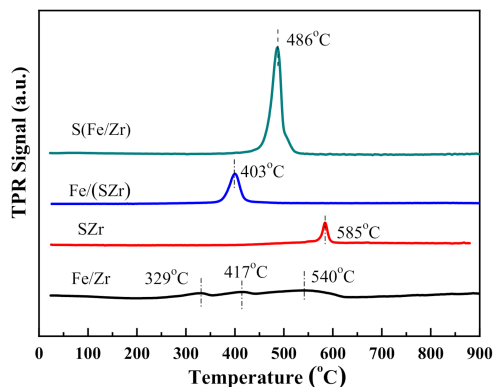

Figure 5. H_2–temperature-programmed reduction (H_2-TPR) patterns of different iron-based catalysts.

2.7. NH_3–TPD

The NH_3–TPD patterns of Fe/(SZr) and S(Fe/Zr) catalysts are shown in Figure 6. One wide NH_3 desorption peak of these three catalysts was displayed in the temperature range of 30–500 °C in the figure. The amounts of NH_3 desorption were different greatly among these two catalysts, and the sequence was following: Fe/(SZr) (38.1 $\mu mol \cdot g^{-1}$) > S(Fe/Zr)(6.3 $\mu mol \cdot g^{-1}$). The NH_3 species desorbed in high temperature range on Fe/(SZr) catalyst reduced a little, but the NH_3 species desorbed in low and medium temperature range increased more greatly than that on the surface of S(Fe/Zr) catalyst, which might be one of the important reason for that Fe/(SZr) catalyst exhibited the higher SCR activity in low and medium temperature range than other catalysts.
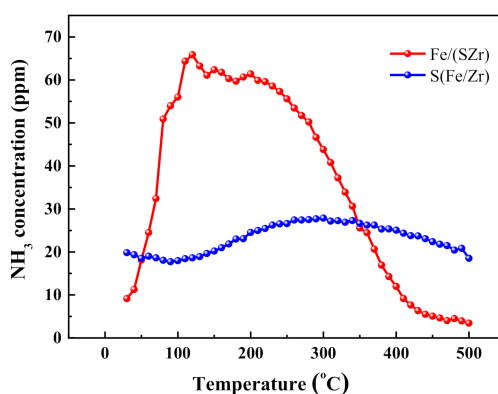

Figure 6. NH_3–TPD profiles of sulfated iron-based catalysts. Reaction conditions: 0.05% NH_3, N_2 balanced, 300 mL/min, and 0.5 g.

2.8. In Situ DRIFTS Studying of the NH_3-Adsorption on Different Catalysts

The in situ DRIFTS spectra of Fe/(SZr) and S(Fe/Zr) catalysts, which were adsorbed and saturated with NH_3 at 30 °C and then purged with N_2, is displayed in Figure 7. Several absorbing vibration peaks

at 3202, 3043, 2840, 1820, 1685, 1600, 1440, and 1257 cm^{-1} appeared over both Fe/(SZr) and S(Fe/Zr) catalysts. Among them, the absorbing vibration peaks at 3202, 3043, and 2840 cm^{-1} were assigned to the N-H bond. For Fe/(SZr) catalyst, the absorbing vibration peaks at 1820 and 1257 cm^{-1} were detected. The absorbing vibration peaks at 1440 and 1257 cm^{-1} of S(Fe/Zr) catalysts were observed. The peaks at 1685 and 1440 cm^{-1} were attributed to the symmetric and asymmetric absorbing vibration adsorbed to Brønsted acid sites [26], while the peaks at 1600 and 1257 cm^{-1} were ascribed to absorbing vibration adsorbed on Lewis acid sites [27,28]. Compared with S(Fe/Zr) catalyst, the peak intensities of absorbed NH$_3$ species bounded to both Brønsted and Lewis acidic sites on the Fe/(SZr) catalyst surface were stronger in the figure. These mainly related to various forms of species on the Fe/(SZr) catalyst, such as isolated Fe$_2$O$_3$, SO$_4^{2-}$, and sulfate species. Fe$_2$O$_3$ could provide Lewis acid sites, whereas SO$_4^{2-}$ supplied Brønsted acid sites, which could adsorb more NH$_3$ species and were in accordance with the results of NH$_3$–TPD.
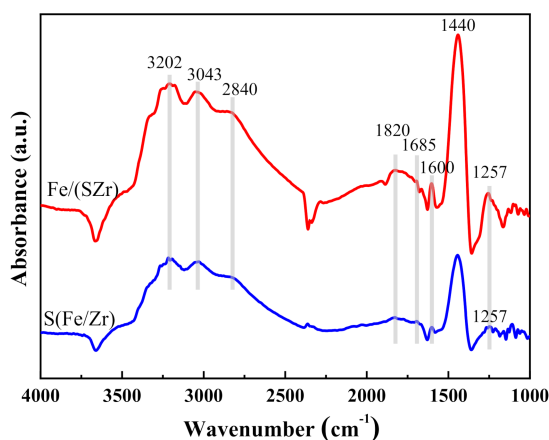

Figure 7. In situ diffuse reflectance infrared Fourier transform spectra (DRIFTS) of Fe/(SZr) and S(Fe/Zr).

2.9. Transient Reaction Studies over Different Catalysts

2.9.1. Transient Reaction Studies over the Fe/(SZr) Catalyst

In Figure 8a, after the sample exposed to NO + O$_2$ reached saturation and was purged with N$_2$ at 250 °C, the nitrate species were stabilized on the surface of Fe/(SZr) catalyst (1525, 1442, 1380, and 1324 cm^{-1}) [29,30]. After NH$_3$ was introduced into the reaction cell, the absorbed NH$_3$ species bounded to different acid sites on catalysts surface were observed (such as the peak at 1608 and 1300 cm^{-1}, which could be attributed to the symmetric and asymmetric stretching vibrational mode of NH$_3$ species on Lewis surface acid sites [31–33]). The peak at 1442 cm^{-1} could be assigned to the symmetric stretching vibration of NH$_4^+$ species bound to Brønsted acid sites [14].) After NH$_3$ was introduced sustainably for 60 min, the adsorbed peaks did not change on the surface of catalysts. These suggested that the nitrate species adsorbed on catalyst surface were active in the SCR reaction, which could react with NH$_3$ existed in air quickly for the redox reaction. As shown in Figure 8b, the stable absorbing peaks attributed to NH$_3$ species were formed over Fe/(SZr) catalyst after introduction of NH$_3$ and purging at 250 °C. (The peaks located at 1608 and 1300 cm^{-1} can be assigned to the symmetric and asymmetric stretching vibrational peaks of NH$_3$ species on Lewis surface acid sites [21,31,33]. The peak at 1430 cm^{-1} can be attributed to the symmetric stretching vibration of NH$_4^+$ species bounded to Brønsted acid sites [34,35].) With the introduction of NO + O$_2$ for 1 min, the NH$_3$ species on catalyst surface became weaker, and the peak at 1631 cm^{-1} related to stretching vibration of NO$_2$ appeared [36,37]. That was to say that the NH$_3$ and oxynitride species can coexist on the surface of catalysts. After introducing NO + O$_2$ for approximately 3 min, the NH$_3$ species almost disappeared and the peaks of stretching vibration of NO$_2$ enhanced. Meanwhile, some steady nitrate species (1324 cm^{-1}) formed on catalyst surface, indicating that NH$_3$ species adsorbed on the surface of catalysts

were active species in the reaction. Overall, both adsorbed nitrate and NH_3 species were active species to proceed SCR reaction.
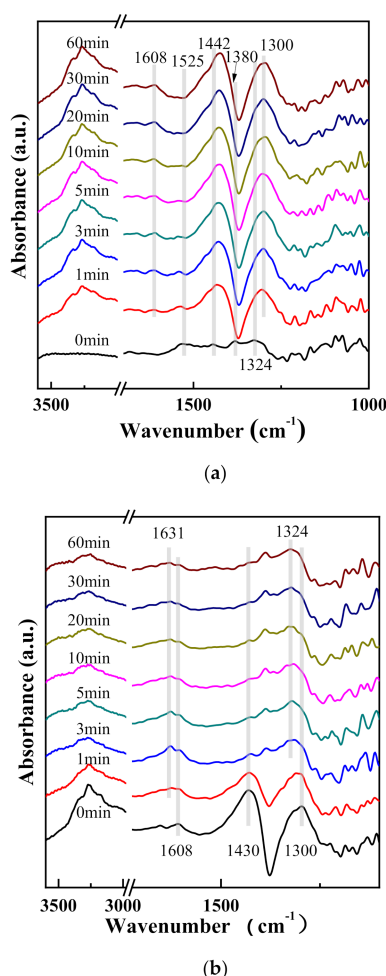

Figure 8. In situ DRIFT spectra of (**a**) NH_3 reacted with preadsorbed $NO + O_2$ and (**b**) $NO + O_2$ reacted with preadsorbed NH_3 on Fe/(SZr).

2.9.2. Transient Reaction Studies over the S (Fe/Zr) Catalyst

When the S (Fe/Zr) catalyst was saturated with $NO + O_2$ and purged with N_2 at 250 °C, a small amount of nitrate species was formed on the surface (1592 and 1334 cm^{-1}). Several absorbing peaks, which were assigned to weakly adsorbed NH_3 species, appeared immediately on catalyst surface after introducing NH_3. (The peaks at 1608 and 1324 cm^{-1} were ascribed to the symmetric and asymmetric stretching vibrational peaks of NH_3 species bounded to Lewis surface acid sites [38]. The absorbing peak at 1429 cm^{-1} was due to the symmetric stretching vibration of NH_4^+ species on Brønsted acid sites [39].) As shown in Figure 9b, steady peaks representing absorbed NH_4^+ species located at 1431 and 1321 cm^{-1} appeared after saturation with NH_3 and purging at 250 °C, which could be attributed to symmetric stretching vibration of NH_4^+ species bounded to Brønsted acid sites [40]. The amount of NH_4^+ species decreased on the catalyst surface after introduction of $NO + O_2$ for 1 min, and then the stretching vibration of H_2O species appeared (1625 cm^{-1}) [41]. The stretching vibration peaks of H_2O enhanced, and the NH_4^+ species still existed at 3 min. After the introduction of $NO + O_2$ for 5 min, the stretching vibration of H_2O species became weaker. Meanwhile, the NO_2 (1637 cm^{-1}) and nitrate species (1540 cm^{-1}) appeared [42–44]. After introducing $NO + O_2$ for 10 min, the NO_2 stretching vibration peaks almost disappeared, but NH_4^+ species remained adsorbed on Brønsted acid sites (1431 and 1321 cm^{-1}) [44]. The NH_4^+ stretching vibration peaks still existed at 60 min, suggesting

that NH_4^+ species adsorbed on the catalyst surface were extremely stable and only a fraction of them participated in the reaction. Therefore, although the NH_3 species on the surface of catalysts could participate in the reaction, the steady NH_4^+ species affected the catalytic activity of SCR reaction. It could be deduced that the SCR reaction on S(Fe/Zr) catalyst surface also followed the E-R pathway: First, NH_3 adsorbed on SO_4^{2-} existed on the catalyst surface to form the NH_4^+ species, which could react with NO_x conducting the oxidation reaction, and further generated N_2 and H_2O.
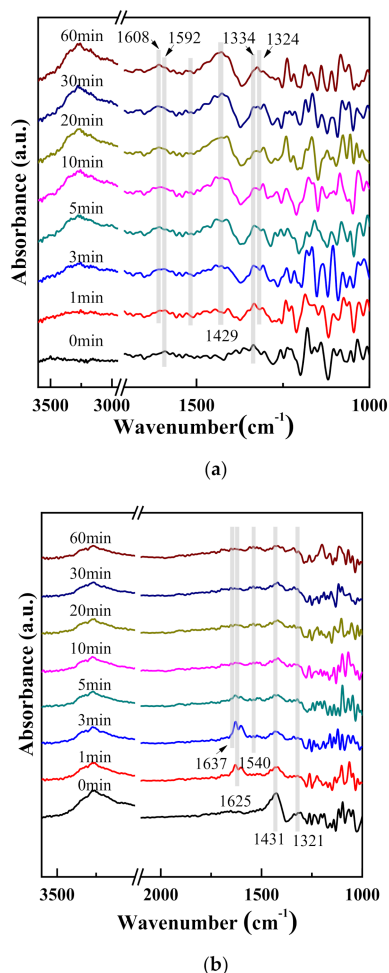

(a)

(b)

Figure 9. In situ DRIFT spectra of (**a**) NH_3 reacted with preadsorbed $NO + O_2$ and (**b**) $NO + O_2$ reacted with preadsorbed NH_3 on S (Fe/Zr).

In conclusion, considering the reaction mechanisms of Fe/(SZr) and S(Fe/Zr) catalysts, it could be inferred that Fe^{3+} and SO_4^{2-} afforded crucial active sites of sulfated iron-based catalysts, and the active species on sulfated iron-based catalyst surface were Fe_2O_3, SO_4^{2-}, and $Fe_2(SO_4)_3$.

3. Discussion

It could be concluded from the results of transient studies that the NH_3-SCR reaction on Fe/(SZr) catalyst followed Langmuir–Hinshelwood (L-H) and Eley–Rideal (E-R) mechanisms. It was not only that the NH_3 species adsorbed on the surface could react with gaseous $NO + O_2$ but also, at the same time, NO_x on the catalyst surface could form large amount of highly active NO_2 species, which could react with adsorbed NH_3 for SCR reaction. The E-R mechanism was executed on S(Fe/Zr) surface in the reaction, which meant that the gaseous NH_3 absorbed first on the surface of catalysts, and then reacted with NO_x in air for redox reaction. Besides, the adsorbed NH_4^+ on catalyst surface was very stabilized and only partly activated to participate in the reaction over the S(Fe/Zr) catalyst.

Combined results of Raman and XPS spectra showed that there were different forms of species on Fe/(SZr) and S(Fe/Zr) catalysts. The existent forms of Fe_2O_3 and SO_4^{2-} on catalysts influenced the mutually coordinated impact on these two catalysts, which determined large differences in the redox ability and adsorption performance of catalysts, and also affected the nitrogen oxide and NH_3 adsorption species participating in the reaction on the catalyst surface. There were more Fe^{3+} and surface-chemisorbed labile oxygen on the surface of Fe/(SZr) catalyst, which facilitated the redox cycle and led to better performance during the reaction. The differences caused the SCR reaction on the surface of Fe/(SZr) and S(Fe/Zr) catalysts to follow different mechanisms, which resulted in the different SCR reaction path on the catalyst surface, and the SCR reaction activity of the catalyst were influenced. Not only the sulfate species but also isolated Fe_2O_3 and SO_4^{2-} ions existed on the Fe/(SZr) catalyst. The isolated Fe_2O_3 on the catalyst was beneficial to the adsorption of sulfate and more NH_3 species on the surface, which promoted the operation of L-H mechanism and the NO_x removal efficiency over Fe/(SZr) catalyst at middle-low temperature. This might be the main reason for the higher catalytic activity of Fe/(SZr) catalyst. For S(Fe/Zr) catalyst, only the SO_4^{2-} and sulfate were existed on the surface. The Fe^{3+} was covered by isolated SO_4^{2-} due to the different orders of loading on S(Fe/Zr) catalyst. The Fe^{3+} ion of the catalyst could not participate well in the redox reaction, so the activity of the catalyst was affected, which explained the reason that the low-temperature activity of the S(Fe/Zr) catalyst was lower than that of the (FeS)/Zr catalyst. In addition, according to the catalytic activity results of the effect of SO_2 on the activity of catalysts at different sulfated positions, the Fe/(SZr) catalyst had poor stability against SO_2 poisoning. The Fe/(SZr) catalyst had Fe_2O_3 species that could promote the activity at medium and low temperature. Meanwhile, Fe_2O_3 easily combined with SO_2 to generate ferrous sulfate or ferric sulfate, occupying the active center, thus leading to the SO_2 poisoning of the Fe/(SZr) catalyst. Therefore, it could be concluded that the different forms of Fe_2O_3 and SO_4^{2-} affected the catalytic activity and caused different mechanisms followed on catalysts. Besides, different species on the surface of catalysts influenced the property of resistance to SO_2 poisoning.

4. Experimental

4.1. Catalyst Preparation

All the catalysts were synthesized through the method of impregnation. The specific experimental steps were as follows: First, the weighed ZrO_2 power was dissolved in distilled water, and some quantities of $Fe(NO_3)_3·9H_2O$ and $(NH_4)_2SO_4$ were added subsequently. Then, the solution was heated to 70 °C. Meanwhile, it was kept stirring till the paste was formed. After that, the paste was dried overnight at 120 °C and calcined under air at 500 °C for 4 h. Finally, several iron-based catalysts with different molar ratios were obtained, signed as Fe_xS_yZr (x = 3, y = 0; x = 0, y = 5; x is the wt.% of Fe_2O_3 and y is the wt.% of SO_4^{2-}). In this paper, Fe3Zr and S5Zr were abbreviated as FeZr and SZr, respectively.

Some SZr power was dissolved and a certain amount of $Fe(NO_3)_3·9H_2O$ was added. Meanwhile, some FeZr catalyst was dissolved and some quantities of $(NH_4)_2SO_4$ were added. These two solutions were heated to 70 °C. Similarly, these solutions were kept stirred until they formed paste and then were dried overnight at 120 °C. Afterwards, they were calcined under air at 500 °C for 4 h. Finally, Fe/(SZr) and S/(FeZr) catalysts were obtained.

4.2. Catalytic Activity Measurement

Measurements of catalytic activity were performed in a fixed-bed quartz reactor with an inner diameter of 9 mm. Precisely, 0.5 g of 40–60 mesh catalysts were used in the reactor. Specific experimental mixture gas conditions were as follows: 500 ppm NO, 500 ppm NH_3, 3 vol.% O_2, and N_2 were used as the balance gas. The total flow rate was 300 mL/min, whereas corresponding small space-time velocity of the gas was approximately 47,000 h^{-1}. The Fourier-transform infrared spectrometer (FT-IR) gas analyzer (Gasmet Dx-4000) was used to measure NO_x, N_2O, and NH_3 concentrations in both the inlet

and outlet. When the catalytic reaction reached a stable state of half an hour at each temperature, the activity data were collected.

4.3. Catalyst Characterization

X-ray diffraction (XRD) was carried out on a D/MAX-RB system with Cu Ka radiation. The diffraction patterns were recorded in the range of 2u from 10° to 90° in steps of 0.018 and 1 s/step.

The Quantachrome Autosorb AS-1 System was used to measure the BET specific surface area, pore size, and pore volume through N_2 adsorption at 77 K.

X-ray photoelectron spectroscopy (XPS) was used to observe chemical valences of catalysts, atomic concentration, and surface species. These experiments were conducted on ESCALab 220i-XL electron spectrometer with radiations of 300 W Mg Ka.

The results of Raman spectra were obtained by using the Raman microscope (InVia reflection, Renishaw), which was equipped with a deep depletion thermoelectric cooled charge-coupled device (CCD) array detector and an advanced Leica microscope (long working distance objective lens 50×).

H_2-temperature-programmed reduction (TPR) curves were recorded through the chemisorption analyzer (Micromeritics ChemiSorb 2720, Micromeritics Norcross, America) using 40 mg of samples. First, samples were pretreated in N_2 at 300 °C for 1 h and then cooled down to the room temperature. Subsequently, using 10% H_2/Ar reducing gas with a flow rate of 50 mL/min, the catalyst was reduced from room temperature to 1000 °C with a temperature gradient of 10 °C/min. The consumed H_2 was calculated by integrating the corresponding TCD signal strength.

NH_3 temperature-programmed desorption (TPD) was performed in a fixed-bed quartz reactor. First, each sample was degassed under the atmosphere of N_2 at 500 °C for 1 h. Second, 500 ppm NH_3 was adsorbed for 1 h after cooling to room temperature. Third, the desorption was carried out in N_2 at the temperature of the last-step response experiment until no NH_3 was detected. Finally, temperature-programmed desorption (TPD stage) was performed at 10 °C/min up to 500 °C. During these experiments, typically, the sample mass of 0.5 g and a gas flow rate of 300 mL/min were needed.

The Nicolet NEXUS 870 FT-IR (Nicolet Madison, America) spectrometer was used to characterize the in situ DRIFTS spectra. Before the experiments, each sample was pretreated at 300 °C for 1 h in N_2 with the flow rate of 100 cm^3/min.

5. Conclusions

The Fe/(SZr) and S(Fe/Zr) sulfated iron-based catalysts synthesized by impregnation methods were investigated in this research. The activities of sulfated iron-based catalysts improved remarkably compared with Fe/Zr catalyst in the temperature range of 250–500 °C. The NO_x conversion and N_2 selectivity exhibited large distinction between Fe/(SZr) and S(Fe/Zr) sulfated iron-based catalysts. The study results revealed that the existence of sulfate, isolated Fe_2O_3, and SO_4^{2-} species on Fe/(SZr) catalyst supplied more acid sites, which could adsorb more NH_3 species and reacted with gaseous NO + O_2. Besides, the reaction between highly active NO_2 species and NO_x on the catalyst surface was beneficial to the catalytic activity. Thus, the SCR reaction on Fe/(SZr) catalyst surface followed both the L-H mechanism and the E-R mechanism. For S(Fe/Zr) catalyst, the SO_4^{2-} and sulfate were existed on the surface. The Fe^{3+} was covered by the independent SO_4^{2-}, so the Fe^{3+} of the catalyst could not participate in the redox reaction well, which affected the progress of the SCR reaction on the catalyst. The absorbed NH_4^+ reacted with NO_x in air and made the S(Fe/Zr) catalyst mainly follow the E-R pathway. In other words, different loading positions of sulfate caused distinctive active components on Fe/(SZr) and S(Fe/Zr) surface, leading to the difference of reaction mechanisms and affected the redox ability and NH_3 adsorption. Therefore, the catalytic activity was affected.

Author Contributions: Writing—original draft preparation, B.F.; writing—review and editing, Z.Z. and Q.L.; supervision, C.L. All authors have read and agree to the published version of the manuscript.

Conflicts of Interest: The authors declare no conflict of interest.

References

1. Long, R.Q.; Yang, R.T. The promoting role of rare earth oxides on Fe-exchanged TiO$_2$-pillared clay for selective catalytic reduction of nitric oxide by ammonia. *Appl. Catal. B* **2000**, *27*, 87–95. [CrossRef]

2. Guo, M.; Liu, Q.; Zhao, P.; Han, J.; Li, X.; Ha, Y.; Fu, Z.; Song, C.; Ji, N.; Liu, C.; et al. Promotional effect of SO$_2$ on Cr$_2$O$_3$ catalysts for the marine NH$_3$-SCR reaction. *Chem. Eng. J.* **2019**, *361*, 830–838. [CrossRef]

3. Liu, C.; Yang, S.; Ma, L.; Peng, Y.; Hamidreza, A.; Chang, H.; Li, J. Comparison on the performance of α-Fe$_2$O$_3$ and γ-Fe$_2$O$_3$ for selective catalytic reduction of nitrogen oxides with ammonia. *Catal. Lett.* **2013**, *143*, 697–704. [CrossRef]

4. Ramis, G.; Yi, L.; Busca, G.; Turco, M.; Kotur, E.; Willey, R.J. Adsorption, activation, and oxidation of ammonia over SCR catalysts. *J. Catal.* **1995**, *157*, 523–535. [CrossRef]

5. Fabrizioli, P.; Bürgi, T.; Baiker, A. Environmental catalysis on iron oxide–Silica Aerogels: Selective oxidation of NH$_3$ and reduction of NO by NH$_3$. *J. Catal.* **2002**, *206*, 143–154. [CrossRef]

6. Long, R.Q.; Yang, R.T. Selective catalytic oxidation of ammonia to nitrogen over Fe$_2$O$_3$-TiO$_2$ prepared with a sol-gel method. *J. Catal.* **2002**, *207*, 158–165. [CrossRef]

7. Long, R.Q.; Yang, R.T. Characterization of Fe-ZSM-5 catalyst for selective catalytic reduction of nitric oxide by ammonia. *J. Catal.* **2000**, *194*, 80–90. [CrossRef]

8. Long, R.Q.; Yang, R.T. Selective catalytic oxidation (SCO) of ammonia to nitrogen over Fe-exchanged zeolites. *J. Catal.* **2001**, *201*, 145–152. [CrossRef]

9. Jung, S.M.; Grange, P. Investigation of the promotional effect of V$_2$O$_5$ on the SCR reaction and its mechanism on hybrid catalyst with V$_2$O$_5$ and TiO$_2$-SO$_4^{2-}$ catalysts. *Appl. Catal. B* **2002**, *36*, 207–215. [CrossRef]

10. Jung, S.M.; Grange, P. Characterization and reactivity of V$_2$O$_5$-WO$_3$ supported on TiO$_2$-SO$_4^{2-}$ catalyst for the SCR reaction. *Appl. Catal. B* **2001**, *32*, 123–131. [CrossRef]

11. Ke, R.; Li, J.; Liang, X.; Hao, J. Novel promoting effect of SO$_2$ on the selective catalytic reduction of NO$_x$ by ammonia over Co$_3$O$_4$ catalyst. *Catal. Commun.* **2007**, *8*, 2096–2099. [CrossRef]

12. Gu, T.; Liu, Y.; Weng, X.; Wang, H.; Wu, Z. The enhanced performance of ceria with surface sulfation for selective catalytic reduction of NO by NH$_3$. *Catal. Commun.* **2010**, *12*, 310–313. [CrossRef]

13. Busca, G.; Lietti, L.; Ramis, G.; Berti, F. Chemical and mechanistic aspects of the selective catalytic reduction of NOx by ammonia over oxide catalysts: A review. *Appl. Catal. B* **1998**, *18*, 1–36. [CrossRef]

14. Wang, H.; Ning, P.; Zhang, Y.; Ma, Y.; Wang, J.; Wang, L.; Zhang, Q. Highly efficient WO$_3$-FeO$_x$ catalysts synthesized using a novel solvent-free method for NH$_3$-SCR. *J. Hazard. Mater.* **2020**, *388*, 121812. [CrossRef] [PubMed]

15. Liu, F.; Asakura, K.; He, H.; Shan, W.; Shi, X.; Zhang, C. Influence of sulfation on iron titanate catalyst for the selective catalytic reduction of NO$_x$ with NH$_3$. *Appl. Catal. B* **2011**, *103*, 369–377. [CrossRef]

16. Zhang, L.; He, H. Mechanism of selective catalytic oxidation of ammonia to nitrogen over Ag/Al$_2$O$_3$. *J. Catal.* **2009**, *268*, 18–25. [CrossRef]

17. Forzatti, P. Present status and perspectives in de-NOx SCR catalysis. *Appl. Catal. A* **2001**, *222*, 221–236. [CrossRef]

18. Liu, C.; Bi, Y.; Li, J. Activity enhancement of sulphated Fe$_2$O$_3$ supported on TiO$_2$–ZrO$_2$ for the selective catalytic reduction of NO by NH$_3$. *Appl. Surf. Sci.* **2020**, *528*, 146695. [CrossRef]

19. Zhu, N.; Shan, W.; Lian, Z.; Zhang, Y.; Liu, K.; He, H. A superior Fe-V-Ti catalyst with high activity and SO$_2$ resistance for the selective catalytic reduction of NO$_x$ with NH$_3$. *J. Hazard. Mater.* **2020**, *382*, 120970. [CrossRef]

20. Tan, W.; Wang, J.; Li, L.; Liu, A.; Song, G.; Guo, K.; Luo, Y.; Liu, F.; Gao, F.; Dong, L. Gas phase sulfation of ceria-zirconia solid solutions for generating highly efficient and SO$_2$ resistant NH$_3$-SCR catalysts for NO removal. *J. Hazard. Mater.* **2020**, *388*, 121729. [CrossRef]

21. Ma, S.; Zhao, X.; Li, Y.; Zhang, T.; Yuan, F.; Niu, X.; Zhu, Y. Effect of W on the acidity and redox performance of the Cu0.02Fe0.2WaTiOx (a = 0.01, 0.02, 0.03) catalysts for NH_3-SCR of NO. *Appl. Catal. B* **2019**, *248*, 226–238. [CrossRef]

22. Chen, J.P.; Yang, R.T. Selective Catalytic Reduction of NO with NH_3 on SO−24/TiO_2 Superacid Catalyst. *J. Catal.* **1993**, *139*, 277–288. [CrossRef]

23. Apostolescu, N.; Geiger, B.; Hizbullah, K.; Jan, M.T.; Kureti, S.; Reichert, D.; Schott, F.; Weisweiler, W. Selective catalytic reduction of nitrogen oxides by ammonia on iron oxide catalysts. *Appl. Catal. B* **2006**, *62*, 104–114. [CrossRef]

24. Ma, L.; Li, J.; Ke, R.; Fu, L. Catalytic performance, characterization, and mechanism study of $Fe_2(SO_4)_3$/TiO_2 catalyst for selective catalytic reduction of NO_x by Ammonia. *J. Phys. Chem. C* **2011**, *115*, 7603–7612. [CrossRef]

25. Liu, J.; Zhao, Z.; Wang, J.; Xu, C.; Duan, A.; Jiang, G.; Yang, Q. The highly active catalysts of nanometric CeO_2-supported cobalt oxides for soot combustion. *Appl. Catal. B* **2008**, *84*, 185–195. [CrossRef]

26. Yang, J.; Ren, S.; Zhou, Y.; Su, Z.; Yao, L.; Cao, J.; Jiang, L.; Hu, G.; Kong, M.; Yang, J.; et al. In situ IR comparative study on N_2O formation pathways over different valence states manganese oxides catalysts during NH_3–SCR of NO. *Chem. Eng. J.* **2020**, *397*, 125446. [CrossRef]

27. Zhan, S.; Zhang, H.; Zhang, Y.; Shi, Q.; Li, Y.; Li, X. Efficient NH_3-SCR removal of NO_x with highly ordered mesoporous $WO_3(\chi)$-CeO_2 at low temperatures. *Appl. Catal. B* **2017**, *203*, 199–209. [CrossRef]

28. Wang, S.; Fan, C.; Zhao, Z.; Liu, Q.; Xu, G.; Wu, M.; Chen, J.; Li, J. A facile and controllable in situ sulfation strategy for CuCeZr catalyst for NH_3-SCR. *Appl. Catal. A* **2020**, *597*, 117554. [CrossRef]

29. Zhang, Q.; Fan, J.; Ning, P.; Song, Z.; Liu, X.; Wang, L.; Wang, J.; Wang, H.; Long, K. In situ DRIFTS investigation of NH_3-SCR reaction over CeO_2/zirconium phosphate catalyst. *Appl. Surf. Sci.* **2018**, *435*, 1037–1045. [CrossRef]

30. Wang, J.; Yan, Z.; Liu, L.; Chen, Y.; Zhang, Z.; Wang, X. In situ DRIFTS investigation on the SCR of NO with NH_3 over V_2O_5 catalyst supported by activated semi-coke. *Appl. Surf. Sci.* **2014**, *313*, 660–669. [CrossRef]

31. Liu, J.; Li, X.; Zhao, Q.; Ke, J.; Xiao, H.; Lv, X.; Liu, S.; Tadé, M.; Wang, S. Mechanistic investigation of the enhanced NH_3-SCR on cobalt-decorated Ce-Ti mixed oxide: In Situ FTIR analysis for structure-activity correlation. *Appl. Catal. B* **2017**, *200*, 297–308. [CrossRef]

32. Chen, C.; Cao, Y.; Liu, S.; Jia, W. The effect of SO_2 on NH_3-SCO and SCR properties over Cu/SCR catalyst. *Appl. Surf. Sci.* **2020**, *507*, 145153. [CrossRef]

33. Song, L.; Yue, H.R.; Ma, K.; Tian, W.; Liu, W.Z.; Liu, C.J.; Tang, S.Y.; Liang, B. Mechanistic aspects of highly efficient Fe_aSbTiO_x catalysts for the NH_3-SCR reaction: Insight into the synergistic effect of Fe and S species. *Ind. Eng. Chem. Res.* **2020**, *59*, 8164–8173. [CrossRef]

34. Shu, Y.; Aikebaier, T.; Quan, X.; Chen, S.; Yu, H. Selective catalytic reaction of NOx with NH_3 over Ce–Fe/TiO_2-loaded wire-mesh honeycomb: Resistance to SO_2 poisoning. *Appl. Catal. B* **2014**, *150–151*, 630–635. [CrossRef]

35. Ma, L.; Cheng, Y.; Cavataio, G.; McCabe, R.W.; Fu, L.; Li, J. In situ DRIFTS and temperature-programmed technology study on NH_3-SCR of NO_x over Cu-SSZ-13 and Cu-SAPO-34 catalysts. *Appl. Catal. B* **2014**, *156–157*, 428–437. [CrossRef]

36. Long, R.Q.; Yang, R.T. Reaction mechanism of selective catalytic reduction of NO with NH_3 over Fe-ZSM-5 catalyst. *J. Catal.* **2002**, *207*, 224–231. [CrossRef]

37. Liu, Z.; Liu, Y.; Li, Y.; Su, H.; Ma, L. WO_3 promoted Mn–Zr mixed oxide catalyst for the selective catalytic reduction of NO_x with NH_3. *Chem. Eng. J.* **2016**, *283*, 1044–1050. [CrossRef]

38. Yan, Q.; Gao, Y.; Li, Y.; Vasiliades, M.A.; Chen, S.; Zhang, C.; Gui, R.; Wang, Q.; Zhu, T.; Efstathiou, A.M. Promotional effect of Ce doping in $Cu_4Al_1O_x$–LDO catalyst for low-T practical NH_3-SCR: Steady-state and transient kinetics studies. *Appl. Catal. B* **2019**, *255*, 117749. [CrossRef]

39. France, L.J.; Yang, Q.; Li, W.; Chen, Z.; Guang, J.; Guo, D.; Wang, L.; Li, X. Ceria modified $FeMnO_x$—Enhanced performance and sulphur resistance for low-temperature SCR of NO_x. *Appl. Catal. B* **2017**, *206*, 203–215. [CrossRef]

40. Shan, W.; Liu, F.; He, H.; Shi, X.; Zhang, C. A superior Ce-W-Ti mixed oxide catalyst for the selective catalytic reduction of NO_x with NH_3. *Appl. Catal. B* **2012**, *115–116*, 100–106. [CrossRef]

41. Wang, Z.-Y.; Guo, R.-T.; Guan, Z.-Z.; Shi, X.; Pan, W.-G.; Fu, Z.-G.; Qin, H.; Liu, X.-Y. The promotion effect of Cr additive on $CeZr_2O_x$ catalyst for the low-temperature selective catalytic reduction of NO_x with NH_3. *Appl. Surf. Sci.* **2019**, *485*, 133–140. [CrossRef]

42. Wang, A.; Guo, Y.; Gao, F.; Peden, C.H.F. Ambient-Temperature NO oxidation over amorphous CrO_x-ZrO_2 mixed oxide catalysts: Significant promoting effect of ZrO_2. *Appl. Catal. B* **2017**, *202*, 706–714. [CrossRef]

43. Liu, H.; Fan, Z.; Sun, C.; Yu, S.; Feng, S.; Chen, W.; Chen, D.; Tang, C.; Gao, F.; Dong, L. Improved activity and significant SO_2 tolerance of samarium modified CeO_2-TiO_2 catalyst for NO selective catalytic reduction with NH_3. *Appl. Catal. B* **2019**, *244*, 671–683. [CrossRef]

44. Gong, P.; Xie, J.; Fang, D.; He, F.; Li, F.; Qi, K. Enhancement of the NH_3-SCR property of Ce-Zr-Ti by surface and structure modification with P. *Appl. Surf. Sci.* **2020**, *505*, 144641. [CrossRef]